Modeling Coupled Evaporation and Seepage in Ventilated Tunnels

T. A.Ghezzehei [*], R. C. Trautz, S. Finsterle, P. J. Cook, and C. F. Ahlers[1]

Earth Sciences Division
Lawrence Berkeley National Laboratory
University of California
MS 90R1116, 1 Cyclotron Rd.,
Berkeley, CA 94720-8126

Manuscript submitted to
Vadose Zone Journal (TOUGH special issue)

---

[*] Corresponding author, Tel (510) 486-5688, Fax (510) 486-5686, Email TAGhezzehei@lbl.gov

[1] Now at *LFR Levine Fricke, Costa Mesa, California*

ABSTRACT

Tunnels excavated in unsaturated geological formations are important to activities such as nuclear waste disposal and mining. Such tunnels provide a unique setting for simultaneous occurrence of seepage and evaporation. Previously, inverse numerical modeling of field liquid-release tests and associated seepage into tunnels were used to provide seepage-related large-scale formation properties by ignoring the impact of evaporation. The applicability of such models was limited to the narrow range of ventilation conditions under which the models were calibrated. The objective of this study was to alleviate this limitation by incorporating evaporation into the seepage models. We modeled evaporation as an isothermal vapor diffusion process. The semi-physical model accounts for the relative humidity, temperature, and ventilation conditions of the tunnels. The evaporation boundary layer thickness (BLT) over which diffusion occurs was estimated by calibration against free-water evaporation data collected inside the experimental tunnels. The estimated values of BLT were 5 to 7 mm for the open underground tunnels and 20 mm for niches closed off by bulkheads. Compared to previous models that neglected the effect of evaporation, this new approach showed significant improvement in capturing seepage fluctuations into open tunnels of low relative humidity. At high relative- humidity values, the effect of evaporation on seepage was very small.

INTRODUCTION

Seepage of liquid water into tunnels is an important phenomenon for subsurface activities such as mining and geologic disposal of nuclear wastes. A key factor affecting the long-term safety of the proposed nuclear waste repository at Yucca Mountain (YM), Nevada, is the seepage of liquid water into waste emplacement tunnels. The rate, chemical composition, and spatial and temporal distributions of seepage are critical factors that determine corrosion of waste canisters, integrity of engineered barriers, and dissolution and mobilization of contaminants and their release to groundwater (Bodvarsson et al., 1999; Finsterle et al., 2003). In unsaturated formations, capillary forces hold the pore water tightly in the formation and prevent it from seeping by gravitational forces into the tunnel – the invisible barrier created by the capillary force is commonly known as a "capillary barrier." Philip and co-workers (Knight et al., 1989; Philip, 1989a; Philip, 1989b; Philip et al., 1989a; Philip et al., 1989b) considered steady-state unsaturated flow around capillary barriers and provided analytical solutions for the critical conditions that trigger seepage into various idealized tunnel goemetries excavated in homogeneous formations. Detailed numerical models have been used to study unsaturated flow in heterogeneous fractured media and seepage into tunnels of various geometries under transient conditions (e.g., Birkholzer et al., 1999; Finsterle, 2000; Finsterle and Trautz, 2001; Li and Tsang, 2003). Site-specific seepage models for the nuclear waste repository at Yucca Mountain, Nevada were developed by calibrating the effective seepage-related parameters against field seepage test data (Finsterle et al., 2003).

Most of the previous numerical models assumed that liquid water leaking into a tunnel drips (seeps) immediately at the place of entry. The potential for evaporation to compete with seepage has been generally ignored, and its effect was lumped with the effective flow parameters

of the unsaturated medium (Finsterle et al., 2003). In calibration of the analytical model of Philip et al. (1989b) against field seepage data, Trautz and Wang (2002) accounted for the effect of evaporation by adjusting the field seepage data for evaporation. Because the data were obtained from tests conducted in relatively humid tunnels, the effect of evaporation on the calibrated seepage-related parameter was not significant. However, recent field measurements of seepage and free-water evaporation in ventilated tunnels at Yucca Mountain have shown that seepage rate is significantly influenced by evaporation. The foregoing discussions suggest that the applicability of models that ignore evaporation is limited to similar humidity and temperature conditions under which the calibrations are performed (Finsterle et al., 2003). Such models cannot satisfactorily capture the seepage rate fluctuations when the seepage experiments are conducted under variable humidity and ventilation conditions. More importantly, seepage models that ignore evaporation, and that are calibrated against seepage data under ventilated and/or low humidity conditions are not expected to perform well in predicting future seepage conditions that are expected to be non-ventilated and humid. The preceding observations call for a calibrated seepage model that reliably performs over a wide range of ventilation and humidity conditions.

The objective of this study is to improve the portability of calibrated seepage models by reducing the impact of evaporation on the calibrated effective parameters. Thus, we propose to incorporate evaporation from tunnel walls into the existing seepage models by assuming a first-order diffusion approximation.

EVAPORATION IN TUNNELS

Fundamentally, evaporation is a two-step process. The first step involves transition from liquid to vapor phase at the liquid-vapor interface (vaporization). The second step is the transport of vapor from the high concentration area at the evaporating surface to the low concentration

area of the ambient air. Accurate modeling of these coupled processes is difficult for several reasons: (1) the first step is a non isothermal phenomenon, and the parameters that govern this process are strongly temperature dependent; (2) the vapor concentration gradient in the boundary layer is strongly influenced by the air flow regime; and (3) the air flow depends on among other things the ambient wind velocity and the roughness of the evaporating surface.

Ho (1997) and Or and Ghezzehei (2000) modeled evaporation from individual water droplets attached to tunnel ceilings, assuming constant temperature and humidity conditions. However, the scale of their approach is too small to be incorporated into the larger scale seepage models that represent the discrete dripping process as a continuum flow. Therefore, the evaporation model required in this study should be of an intermediate scale and be compatible with the existing seepage models. The formulation used herein capitalizes on the observed dependence of evaporation rate on tunnel humidity and ventilation conditions, and the availability of high resolution time-series data of relative humidity, temperature and free-water evaporation rate (Trautz and Wang, 2002).

In the following subsections, we introduce an isothermal vapor diffusion model of evaporation and define the problem domain and boundary conditions. This is followed by estimation of the evaporation model parameters, using free-water evaporation data. Finally, a remark on evaporation from porous surface is provided.

Isothermal Vapor Diffusion Model

To simplify the first step of evaporation (vaporization) we assume the following: (1) the absorption of latent heat and its effect on the physical properties of the liquid-vapor interface are ignored; (2) the time dependence of the vaporization process (e.g., Zhang and Wang, 2002; Zhang et al., 2001) is neglected; and (3) the vapor partial pressure of the interfacial air is

assumed to be under thermodynamic equilibrium. At equilibrium, the air above a flat surface of pure water is considered saturated with vapor; its vapor pressure is denoted by p_s. This saturation vapor pressure rises with temperature. In the temperature range of –10°C to 50°C, the saturation vapor pressure is related to interfacial temperature by (Murray, 1966):

$$\ln p_s = a\frac{T}{T+b} + c \qquad [1]$$

where $a = 21.87$, $b = 265.5\,°\mathrm{C}$ and $c = 6.41$ are constants, and T is the interfacial temperature. For non-flat interfaces (such as capillary menisci) the actual interfacial vapor pressure p is related to the interfacial capillary potential by the classic Kelvin equation,

$$\ln\left(\frac{p}{p_s}\right) = P_C \cdot \frac{M_W}{\rho_W R\, T} \qquad [2]$$

where P_C is the capillary pressure, ρ_W and M_W are the density and molecular mass of liquid water, respectively, and R is the universal gas constant. Note that the relative humidity of air is defined as the ratio of the actual partial pressure (p) to the saturated vapor pressure (p_s)

$$h = p/p_s \qquad [3]$$

The second step of evaporation, vapor removal from the interface, is modeled as a first-order phenomena described by Fickian diffusion (Rohsenow and Choi, 1961). In one dimension and under constant temperature, the vapor flux (J_v) is given by

$$J_V\big|_T = -D_V \cdot \frac{\mathrm{d}C}{\mathrm{d}z} \qquad [4]$$

where D_V is the vapor diffusion coefficient, which is related to the ambient air pressure (P) and air temperature (T) by

106 $$D_V = 2.13\times10^{-5}\frac{10^5}{P}\left(\frac{T}{273.15}\right)^{1.8} \quad [5]$$

107 and the vapor concentration C is related to vapor pressure by

108 $$C = \frac{M_W}{RT}\cdot p \quad [6]$$

109 In the subsequent subsection, we define the problem domain and develop the appropriate
110 boundary conditions needed to solve the vapor diffusion equation [4].

111 ## Velocity and Concentration Boundary Layers

112 In admitting diffusive flux as the primary mechanism for vapor removal from the
113 evaporating surface, we tacitly assume that airflow above the evaporating surface is fully
114 developed and laminar, as illustrated in Fig. 1a. The free-stream air velocity (V^∞) is retarded in
115 the vicinity of the evaporating surface because of frictional resistance. The air velocity parallel to
116 the evaporating surface increases from $V = 0$ at $z = 0$ (no-slip) asymptotically to $V = V^\infty$ at a
117 distance sufficiently far away from the surface. For fully laminar flow conditions, the thickness
118 of the boundary layer of retarded velocity (defined as $V \le 0.99V^\infty$) is inversely proportional to
119 the square root of the free-stream velocity (Rohsenow and Choi, 1961):

120 $$\delta_V \propto 1/\sqrt{V^\infty} \quad [7]$$

121 Because the equations that describe laminar air flow parallel to a flat surface and
122 diffusion from a flat surface are analogous (Rohsenow and Choi, 1961), a similar notion of
123 concentration boundary layer holds near the evaporating surface. The vapor concentration profile
124 is illustrated in Fig. 1b. The vapor concentration decreases from an equilibrium value ($C = C^0$) at
125 $z = 0$ to a value determined by the free-stream humidity at sufficiently far distance. The

concentration boundary layer thickness (δ_C) is related to the velocity boundary layer thickness by the Schmidt number,

$$Sc = \frac{\delta_C}{\delta_V} = \frac{\mu_a}{\rho_a \cdot D} \quad [8]$$

where μ_a and ρ_a are the viscosity and density of air, respectively. At 20 °C and 1 atm pressure, the Schmidt number is approximately unity. In the remainder of this paper the subscripts in the boundary layer thickness are dropped and $\delta = \delta_V = \delta_C$. It is evident from [7] and [8] that the concentration BLT (δ) is inversely related to the square root of the free-stream velocity (V^∞) and can serve as a direct measure of the tunnel ventilation condition. In a subsequent subsection, estimation of the BLT will provide further elaboration on the dependence of δ on ventilation conditions.

Fig. 1. Schematic description of (a) air velocity and (b) vapor concentration profiles above a free water surface

Boundary Conditions

The domain of the vapor diffusion equation [4] is the concentration boundary layer introduced in the preceding subsection. The boundary condition on [4] corresponding to the equilibrium vapor concentration at the evaporating surface ($z = 0$) is given by (using [2] and [6]):

$$C = C^0 = \frac{M_W}{R\,T}\, p_s\, \mathbf{exp}\left[\frac{P_C}{\rho_W}\frac{M_W}{R\,T}\right] \quad [9]$$

The second boundary condition is at the border of the concentration boundary layer $z = \delta$, where the vapor concentration is defined by the relative humidity (h) of the ambient air:

$$C = C^{\infty} = \frac{M_W}{R\,T}\, p_s\, h \qquad [10]$$

If the boundary conditions change slowly, the evaporation rate can be considered to be at steady state and the concentration gradient $\mathbf{d}\,C/\mathbf{d}\,z$ is constant throughout the boundary layer. Then, the steady state vapor diffusion equation [4] under isothermal conditions is simplified to

$$J_V = -D_v \cdot \frac{C^0 - C^{\infty}}{\delta} \qquad [11]$$

Note that the ratio δ/D_v is commonly referred to as aerodynamic resistance. The isothermal vapor diffusion equation [11] is considered valid for modeling evaporation from tunnel surfaces and free water. Fujimaki and Inoue (2003) found [11] (also known as the bulk transfer equation) to be valid in laboratory evaporation experiments in which the ambient air velocity was on the order of 1 m/s. All the variables of this model are directly related to physical conditions in the tunnel, and all of them, except δ, can be independently determined from measured quantities. The boundary-layer thickness (δ) can be estimated by calibrating [11] against free water evaporation data, as discussed in the next subsection.

Estimation of the Boundary-Layer Thickness

Apart from the capillary pressure at the evaporating surface, evaporation from free water and that from a wet porous surface are thus far assumed to be identical processes. Therefore, a controlled evaporation experiment from a still water surface can be used to estimate the vapor concentration boundary layer thickness, which is also applicable to evaporation from wet tunnel surfaces at similar ventilation conditions. Upon substitution of [1], [5], [9], and [10] in [11], and noting that the capillary pressure of the free water surface is $P_C = 0$, we arrive at a free-water evaporation equation,

$$J_V = -2.13\times10^{-5}\frac{10^5}{P}\left(\frac{T}{273.15}\right)^{1.8}\cdot\left(a\frac{T}{T+b}+c\right)\cdot\frac{M_w}{RT}\frac{1-h}{\delta} \quad [12]$$

According to the isothermal assumption, T denotes the temperature of the evaporating surface and the surrounding air. Assuming the change in conditions that affect evaporation rate is slow compared to the time it takes to reach steady-state evaporation, [12] can be fitted to time-series data of evaporation rate data, measured at known temperature, pressure, and relative humidity conditions. The best-fit δ represents the boundary-layer thickness at the prevailing ventilation condition. However, it should also be noted that uncertainties associated with the assumed simplifications (including isothermal conditions, flat evaporating surface, and laminar airflow) are lumped in this parameter. Thus, the boundary-layer thickness should be considered an effective parameter.

Evaporation from Porous Surface

The surface of an unsaturated porous medium typically consists of solid (matrix of the medium) and pore/fracture (liquid and gas) components, rendering the evaporating surface heterogeneous with respect to vapor concentration, as illustrated in Fig. 2a. During seepage, however, tunnel ceilings are usually covered with liquid films (e.g., Trautz and Wang, 2001), and the vapor concentration could be considered locally homogeneous. For simplicity, we extend this assumption of locally uniform distribution of vapor concentration to the entire tunnel Fig. 2b. The vapor concentration at any given location on the tunnel is assumed to be at capillary equilibrium with the pores and fractures of the porous medium. The datum $z = 0$ for the vapor diffusion is set on the surface of the tunnel (as illustrated in Fig. 2b). Although this assumption is likely to fail at very low saturations (when the liquid is scattered in a few fine pores and

188 fractures) it is expected to be of marginal consequence because the evaporation rate under such
189 conditions is very low.

190 Fig. 2. Evaporating surface area of a porous medium: (a) partitioning of the surface into non-
191 evaporating solid and evaporating pores; (b) proposed approach of uniform gas-phase
192 surface. The dark shade denotes vapor in pores and/or fractures.

193 ## COUPLED SEEPAGE AND EVAPORATION

194 In a tunnel constructed in unsaturated formations, the flow velocity of water in the rock is
195 usually stagnated near the crown, resulting in elevated moisture (Philip et al., 1989b). Unlike
196 evaporation from ground surface, where infiltration opposes the evaporation flux, the condition
197 in tunnels is favorable for simultaneous occurrence of evaporation and seepage. Field tests that
198 exhibit simultaneous evaporation and seepage are described below. After field test descriptions,
199 we present a brief description of seepage modeling using the numerical simulators TOUGH2
200 (Pruess et al., 1999) and iTOUGH2 (Finsterle, 1999) and discuss implementation of evaporation
201 in these models.

202 ### Field Tests

203 The data reported in this paper were obtained from field tests and measurements
204 conducted at the proposed nuclear waste repository at Yucca Mountain currently under
205 investigation by the US Department of Energy (DOE). Air-injection tests were conducted to
206 characterize the permeability and small-scale heterogeneities of the formation, and liquid-release
207 tests were performed to study seepage phenomena. Relative humidity, temperature, and free-
208 water evaporation were monitored at the test site to assess the evaporation conditions. Detailed
209 description of the site and tests conducted at the site are provided elsewhere (Birkholzer et al.,

1999; Bodvarsson et al., 1999; Finsterle and Trautz, 2001; Finsterle et al., 2003; Trautz and Wang, 2001; Trautz and Wang, 2002; Wang et al., 1999). This study is concerned with the lower lithophysal welded tuff unit at Yucca Mountain, in which about 80% of the proposed repository is expected to reside. This unit contains many small fractures (less than 1 m long) and is interspersed with numerous lithophysal cavities (0.15 m–1 m in diameter).

In the lower lithophysal unit, an 800-m long drift (5 m in diameter) for enhanced characterization of the repository block (ECRB) was excavated off the main Exploratory Studies Facility (ESF) tunnel. Liquid-release and air-injection tests were systematically conducted in this ECRB Cross Drift along boreholes drilled into the ceiling of the Cross Drift at regular intervals. Similar tests were conducted in a short (approximately 15 m long) drift excavated off the Cross Drift (niches). Schematic alignment of the tunnels is shown in Fig. 3a. This paper is concerned with tests conducted at a Cross Drift borehole designated as LA#2 (Fig. 3b) and a short drift known as Niche 5 (Fig. 3c). The tests and measurements conducted in the Cross Drift and Niche 5 are briefly described below.

Air-injection tests

The purpose of the air-injection tests was to estimate absolute permeability of the formation as a basis for the stochastic generation of heterogeneous permeability fields. Short sections of the boreholes (0.3 m in Niche 5, 1.8 m in Cross Drift) were isolated using an inflatable packer system, and compressed air was injected. Air injection was terminated when steady-state pressure was reached. Air-permeability values were derived from the steady-state pressure data according to an analytical solution of LeCain (1995). Permeabilities determined from air-injection tests were considered representative of the absolute permeability of the test interval.

Liquid-release Tests

Liquid release tests were conducted in boreholes drilled above tunnels to evaluate seepage into waste emplacement drifts. The alignment of the boreholes and test intervals are schematically shown in Fig. 3. The liquid release boreholes in the Cross Drift were approximately 20 m long, drilled into the ceiling of the Cross Drift at a nominal inclination of 15° from the horizontal. Liquid release data from a borehole designated as LA#2 were used in this study. The borehole was partitioned into three zones (designated as Zone 1, Zone 2, and Zone 3) available for liquid release testing. The distances from the middle of the liquid-release zones to the drift crown were 1.58 m, 2.84 m, and 4.10 m for Zone 1, Zone 2, and Zone 3, respectively. The liquid release boreholes in Niche 5 were near horizontal. Of the six boreholes available for tests, data from boreholes #4 and #5 were used in this study. The liquid release tests were performed by injecting water into a test interval isolated by inflated rubber packers. Water that seeped into the tunnels was captured and measured using automated recording devices.

Relative Humidity and Temperature Measurements

The Cross Drift was actively ventilated during regular working hours, thus the relative humidity of the tunnel was usually low. To mitigate the effect of evaporation in the seepage process, the seepage collection interval was guarded using curtains on both ends. Because Niche 5 was isolated from the actively ventilated Cross Drift by a bulkhead, the relative humidity was relatively high. To aid in the estimation of evaporation during the liquid release tests, the relative humidity and temperature of the air inside and outside of the curtains (for the Cross Drift) and in front of and behind the bulkhead (for Niche 5) were monitored.

The evaporation rate from still water was measured by monitoring the level (mass) of water in evaporation pans placed within the space enclosed by the seepage capture tray and end curtains (for the Cross Drift tests) and behind the bulkhead (for Niche 5).

Fig. 3. Schematic alignment of tunnels and boreholes: (a) parts of the Exploratory Studies Facility (ESF) tunnel and Enhanced Characterization of the Repository Block (ECRB) cross-drift; (b) liquid release test setup in the Cross Drift, including liquid release intervals and liquid injection and seepage collection equipment; and (c) vertical section of Niche 5 along with location of all the test boreholes.

TOUGH2/iTOUGH2 Seepage Model

A detailed description of the numerical models developed for flow in fractured formation around a tunnel and associated seepage into the tunnel using TOUGH2/iTOUGH is given by Finsterle et al (2003). A summary follows.

The TOUGH2 code is an integral finite difference simulator that represents unsaturated flow at the scale of individual grids by Richards' equation (Bear, 1972; Pruess et al., 1999)

$$\phi \rho \frac{\partial}{\partial t} S_e = \mathrm{div}\left[k \frac{\rho}{\mu} \nabla \left(P_C + \rho g z \right) \right] \qquad [13]$$

The appropriateness of using this continuum approach to simulate water flow through unsaturated fractured rock was shown by Finsterle (2000). The effective permeability (k) and capillary pressure (P_C) are functions of liquid saturation as given by van Genuchten's models (1980)

$$k = k_a \, S_e^{1/2} \left[1 - \left(1 - S_e^{1/m} \right)^m \right]^2 \qquad [14]$$

$$P_C = -\frac{1}{\alpha}\left[S_e^{-1/m} - 1\right]^{1-m} \quad [15]$$

where k_a is the absolute permeability, $1/\alpha$ and m are fitting parameters with $\alpha > 0$ and $0 < m < 1$, and the effective saturation, S_e, is defined as $S_e = (S - S_{lr})/(1 - S_{lr})$, with S_{lr} being the residual liquid saturation. While the k_a values were considered spatially heterogeneous, the $1/\alpha$, m, and S_{lr} parameters were summed to be homogeneous for a given test bed (Finsterle et al., 2003). The absolute permeability, k_a, was derived from the air-injection tests. The van Genuchten m parameter and the residual saturation were taken to be $m = 0.608$ and $S_{lr} = 0.01$, respectively (Finsterle et al., 2003). The van Genuchten capillary strength parameter $1/\alpha$ was estimated through inverse modeling. In the numerical seepage model, the condition for seepage is determined by the total water-potential gradient at the connection between the porous medium and the tunnel, as depicted in Fig. 4. The flow rate along the connection between the porous medium and the tunnel is given by

$$q_z = k\frac{\rho}{\mu}\frac{\Delta P + \rho g z}{\Delta z} \quad [16]$$

where ΔP denotes the capillary pressure difference across the distance between the last formation node and the tunnel node Δz. The nodal distance Δz is chosen to be a representative of the average length of fractures intersecting the tunnel that are not draining laterally (Finsterle et al., 2003). From [16], and assuming that the capillary pressure in the opening is zero, it follows that downward seepage ($q_z > 0$) occurs only when the following condition is satisfied:

$$-P_C^{\,*} > \rho g \Delta z \quad [17]$$

where $P_C^{\,*}$ is the threshold capillary pressure at the last node adjacent to the opening. The critical capillary pressure $P_C^{\,*} = -\rho g \Delta z$ depends on the grid size or nodal distance of the numerical

model. According to [17], the tunnel surface does not need to be fully saturated for seepage to commence as in the case of unfractured homogeneous porous media (Philip et al., 1989b).

Fig. 4. Schematic description of the seepage and evaporation connections between nodes that represent the rock of the tunnel wall and the tunnel.

Implementation of Evaporation in TOUGH2

While seepage occurs only when the critical condition given in [17] is satisfied, vapor flow from/to tunnel walls to/from tunnel air occurs as long as there is vapor pressure disequilibrium between them. Coupling of the seepage and evaporation processes is illustrated in Fig. 4. Mass-transfer rate of water, including seepage, is represented in TOUGH2 by equations similar to [16], where the driving force is pressure gradient. To incorporate evaporation into the existing model without significant changes to the governing flow equations, we must rewrite the concentration-gradient dependent diffusion equation [11] in the form of equation [16]. Noting that the connection length Δz denotes the vapor concentration boundary layer thickness δ, the equivalent evaporative permeability can be written as

$$k_{eq} = D_v \frac{\mu}{\rho} \left(\frac{C^0 - C^\infty}{P_C{}^0 - P_C{}^\infty} \right) \qquad [18]$$

where the variables with a superscript of 0 correspond to the tunnel wall and those with a superscript of ∞ denote the tunnel air. The capillary pressure of the tunnel $P_C{}^\infty$ is equivalent to the relative humidity [3] of the tunnel, as described by Kelvin's equation [2]. The vapor concentrations are computed according to [11] and [12]. Equation [18] was implemented in TOUGH2 as a special evaporation connection. When the conditions for both evaporation and

seepage permit, the total mass flow from the tunnel wall to the tunnel is considered as the sum of both.

Numerical Meshes

Different numerical models were constructed to simulate liquid-release tests and seepage into the underground openings at different test locations. Three-dimensional meshes of the test sites were generated with grid sizes of 0.3 m × 0.1 m × 0.1 m for the Cross Drift and 0.1 m × 0.1 m × 0.1 m for Niche 5 (see Fig. 5). For the Cross Drift meshes, a circular cylindrical tunnel of 5 m diameter was removed from the center of the mesh to represent the tunnel. Only one half of the symmetric mesh was used in the simulations to save computational load. For the Niche 5 meshes, surveyed niche geometry was removed from the numerical mesh to replicate the test sites. The liquid-release boreholes are indicated in Fig. 5 by bold black lines, and the white sections at the middle of the boreholes represent the injection intervals. The Cross Drift borehole is inclined while the Niche 5 boreholes are parallel to the centerline of the niche. The Cross Drift mesh in Fig. 5a represents the Zone 2 test interval. In Fig. 5b and Fig. 5c, boreholes #4 and #5 are revealed, respectively (see also Fig. 3c). Notice that the injection intervals in boreholes #4 and #5 are located at 3–3.5 m and 8.5–8.8 m, respectively, from the borehole collars; hence, the respective tunnel outlines are different.

Fig. 5. Numerical meshes of (a) Niche 5 with borehole #4, (b) Niche 5 with borehole #5, and (c) the Cross Drift, along with a typical realization of the correlated stochastic permeability field. Bold black lines denote the liquid-release boreholes, and the white section in the middle of the boreholes is the injection interval.

The spatial structure of the Niche 5 permeability data was analyzed using the GSLIB module GAMV3 (Deutsch and Journel, 1992) and a spherical semivariogram was fitted to the resulting variogram. Because only six permeability data were available from the Cross Drift, assumed spherical variogram parameters were used. Recall that the permeability of the Cross Drift was measured on 1.8 m long intervals of the boreholes, and the standard deviation of the measured data was 0.21. The variability of the permeability on the scale of the 0.3 m long gridblock was expected to be greater than the measurement interval. For the purpose of generating a heterogeneous field, the permeability was taken to be log-normally distributed with a variance (sill) value of 1 order of magnitude. Computed and prescribed geostatistical parameters (Table 1) were used to generate spatially correlated permeability fields, using the sequential indicator simulation (SISIM) module of the GSLIB (Deutsch and Journel, 1992). Multiple realizations of the permeability field were generated and mapped to the numerical meshes. Representative permeability field realizations for the Cross Drift and Niche 5 are shown in Fig. 5.

Table 1. Mean, standard deviation, and correlation length of log-permeability data collected in the Cross Drift and Niche 5. The values in parentheses are prescribed values because the number of measurements was not adequate to compute the respective parameters.

Location	*n*	Mean log (k) [m^2]	Std. Dev. [m^2]	Spherical Variogram		
				Sill Value [$log(k)^2$]	Correlation length [m]	Nugget effect [$log(k)^2$]
Niche 5	61	-10.95	1.31	1.81	0.91	0.02
Cross Drift	6	-10.73	0.21	1.0	0.2	-

The tunnels were represented in the seepage models by two types of overlapping gridblocks, one corresponding to seepage and the other to evaporation. The seepage gridblocks were assigned a zero capillary pressure, whereas the evaporation gridblocks were assigned a capillary pressure and vapor concentration corresponding to the tunnel relative humidity of the tunnel, as given by [2] and [3]. No-flow boundary conditions are specified at the left, right, front, and back sides of the model. A free-drainage boundary condition is applied at the bottom to prevent an unphysical capillary boundary effect.

RESULTS AND DISCUSSIONS

Evaporation Boundary Layer

The evaporation data collected in Niche 5 were used to calibrate the evaporation model. The data were grouped into three classes based on airflow velocity (ventilation): (1) inside Niche 5 without ventilation; (2) outside Niche 5 with active ventilation; and (3) outside Niche 5 without active ventilation, the regime usually encountered during nights and weekends. In Fig. 6, the measured relative humidity, and temperature, and evaporation rates from still water are plotted. The evaporation model [12] was fitted to the measured data by adjusting the boundary layer thickness. The best-fit estimates of the boundary layer thickness are listed in Table 2.

Fig. 6. Temperature, humidity, and evaporation rate data, along with model fit of the evaporation data for inside and outside of Niche 5.

In agreement with the theoretical assessment (Equation [7]), the estimated δ showed an inverse relationship with the ventilation conditions. Inside Niche 5, the air was the calmest because it was isolated from the Cross Drift by a bulkhead (see Fig. 3). As a result, the thickest boundary layer (20 mm) was obtained inside Niche 5. Fig. 6 shows that the relative humidity

outside Niche 5 increases at nights and during weekends when active tunnel ventilation is turned off. However, this increase in relative humidity is insufficient to explain the observed decrease in evaporation. Therefore, as shown in Fig. 6, reduced air ventilation during nights and weekends is also accompanied by an increase in the thickness of the boundary layer. The estimated boundary-layer-thickness values and Equation [7] suggest that the air velocity outside Niche 5 is higher than the inside by factors of 7 (without active ventilation) and 16 (with active ventilation). These results confirm the applicability of Equation [12] to describe the effects of humidity, temperature, and ventilation on evaporation rate.

Table 2. Summary of estimated boundary layer thickness for Niche 5 and their application.

Location of Experiment	**δ (mm)**	**Used For Simulation of Liquid-Release Tests in**
Inside Niche 5	20.0	Niche 5
Outside Niche 5, ventilation off	7.5	Cross Drift (with end curtains)
Outside Niche 5, ventilation on	5.0	Not used

Coupled Seepage and Evaporation

In this section, simulations of coupled seepage and evaporation are compared with measured seepage rate data. The software iTOUGH2 (Finsterle, 1999) was used to match the simulated seepage rate with the measured values by adjusting the free capillary strength parameter ($1/\alpha$) (Finsterle et al., 2003). The corresponding evaporation rate from the tunnel walls simulated using the tunnel relative humidity and calibrated boundary layer thickness.

Niche 5

Here, two different data sets from liquid release tests conducted in boreholes #4 (October, 2002) and #5 (July 2002) are compared with the Niche 5 seepage models. The liquid release rate, seepage rate, and relative humidity data as well as modeled liquid release rate and fitted seepage rate are shown in Fig. 7. The best-fit $1/\alpha$ values were 671 ± 223 Pa and 740 ± 339 Pa for boreholes #4 (30 inversions) and #5 (24 inversions), respectively. The measured seepage rates attained a steady-state flow rate after several days. Because the early-time transient data are biased by storage (e.g., in lithophysal cavities and matrix) and/or fast flow paths connecting the injection interval to the tunnel ceilings, the model was fitted to the late-time steady state data. In the simulations, the relative humidity was kept constant at 0.85 to match with the lowest steady-conditions observed during the borehole #4 tests.

Fig. 7. Calibration of seepage-rate data from liquid-release tests conducted in Niche 5. Calculated seepage rate curves show only one of the multiple inversions.

To quantify the impact of evaporation on seepage over the observed high relative humidity range (0.85–0.99), the calibrated seepage model of borehole #4 was used to simulate seepage and evaporation at relative humidity values of 0.85, 0.95, and 0.99. The resulting steady state seepage and evaporation rates (on Day 10) are plotted as percentages of the liquid release rate in Fig. 8. At a relative humidity of 0.85, the evaporation rate from the entire niche wall surface and the seepage rate are comparable in magnitude. As the relative humidity was increased, the steady-state evaporation rate showed a drastic decrease, while the corresponding seepage rate increased only slightly. Thus, at these high relative humidity conditions, the main impact of evaporation is on the quantity of liquid diverted around the tunnel.

Fig. 8. Effect of high relative humidity on evaporation and seepage rates.

ECRB Cross Drift

In this subsection, two different data sets from liquid release tests conducted in borehole LA2, Zone 2 and Zone 3, are compared with the ECRB Cross Drift seepage model. The liquid release rate, seepage rate, and relative humidity data, as well as modeled liquid-release rates and fitted seepage rates, are plotted in Fig. 9. The best-fit capillary-strength parameter $1/\alpha$ were 557 ± 56 Pa for zone 2 and 535 ± 58 Pa for zone 3, based on 21 and 19 inversions, respectively. Note that both of the liquid-release tests were conducted concurrently. The measured and simulated seepage rate fluctuations were strongly correlated to the drastic changes in relative humidity (hence, evaporation). The model captured this evaporation effect satisfactorily, tracking increases in measured seepage rates as relative humidity increases and vice versa.

Fig. 9. Calibration of seepage-rate data from liquid-release tests conducted in the ECRB Cross Drift. Calculated seepage rate curves show only one of the multiple inversions.

The interplay between relative humidity fluctuation and dynamics of flow and ceiling wetness at different times during the test in Zone 2 are visualized in Fig. 10. During this test, the liquid release rate was relatively stable (steadily increasing from 31 mL/min on Day 0 to 34 mL/min on Day 34). However, the relative humidity fluctuated between 30% and 90% during this period. Fig. 10 shows snapshots of the liquid saturation distribution on Days 0, 10, 20, and 30. Just before the test began, the drift wall has dried out because of the low relative humidity in the drift. The liquid saturation at this time was in equilibrium was the assumed background percolation flux of 2 mm/yr. On day 10 day of injection (relative humidity ~ 70%), water reached the crown of the drift, seepage has started, water was being diverted around the drift, and

436 wet plume has reached approximately to the elevation of the spring line. After 20 days, however,
437 the plume has shrunk significantly because of reduced humidity (approximately 12%) and
438 increased evaporation. Moreover, the seepage rate and seepage locations (indicated by inverted
439 triangles) have decreased. Before the 30-day time mark, the relative humidity rose up to
440 approximately 80%; thus, the evaporation rate was reduced, the wet plume grew, and seepage
441 rate and number of seeps increased. In general, despite the high liquid release rate, the flow
442 regime remained unsaturated. The liquid saturation was highest near the drift crown, which
443 induces a capillary pressure gradient that promoted flow diversion around the drift (capillary
444 barrier effect). Seepage and evaporation removed water from the formation as water flows
445 around the drift, limiting the spread of the wetted region on the drift wall.

446 Fig. 10. Liquid saturation distribution simulated with model calibrated against seepage-rate data
447 from liquid-release tests conducted in the Cross Drift borehole LA#2, Zone 2 at 0, 10,
448 20, and 30 days after the start of the liquid release tests. Note the correlation of tunnel
449 wall wetness to tunnel relative humidity.

450 ## SUMMARY AND CONCLUSIONS

451 In this paper, we (1) estimated the evaporative boundary-layer thickness by calibrating a
452 semi-physical evaporation model, which considers isothermal vapor diffusion; (2) calibrated a
453 heterogeneous fracture-continuum model against seepage-rate data; and (3) tested the effect of
454 evaporation on seepage predictions. The major conclusions of this study are listed below:

455 1. The simplified vapor-diffusion approach of modeling evaporation was found to be effective
456 in capturing the roles of the important environmental conditions that affect evaporation –
457 namely, relative humidity, temperature, and ventilation. Calibrated thicknesses of the

evaporation boundary layer were obtained for three ventilation conditions representing the conditions at the liquid-release test sites at Yucca Mountain.

2. We found that evaporation reduces seepage significantly in tests conducted under ventilated conditions. Therefore, it is important to account for evaporation effects when calibrating a seepage process model against liquid-release-test data collected under ventilated conditions. In contrast, the impact of evaporation on seepage rate was minimal in closed-off niches, where relative humidity values were generally high. Thus, when using data obtained from closed-off and/or artificially humidified niches, ignoring the effect of evaporation is expected to introduce little error in the estimation of seepage-relevant parameters.

3. The classification of ventilation regimes is based on crude assessment of the tunnel environment. Bearing of external wind velocity variations (note that the Cross Drift is connected to the air outside the ESF) was not accounted for. The matching between measured evaporation rate and model predictions can be improved if accurate measurement of air velocity in the tunnels was made.

ACKNOWLEDGMENT

We thank Jens Birkholzer and Guomin Li for their thorough reviews and insightful comments. This work was supported by the Director, Office of Civilian Radioactive Waste Management, U.S. Department of Energy, through Memorandum Purchase Order EA9013MC5X between Bechtel SAIC Company, LLC, and the Ernest Orlando Lawrence Berkeley National Laboratory (Berkeley Lab). The support is provided to Berkeley Lab through the U.S. Department of Energy Contract No. DE-AC03-76SF00098.

480

481

482

REFERENCES

Bear, J., 1972. Dynamics of fluids in porous media Elsevier, New York, New York.

Birkholzer, J., G.M. Li, C.F. Tsang, and Y. Tsang, 1999. Modeling studies and analysis of seepage into drifts at Yucca Mountain. Journal of Contaminant Hydrology 38:349-384.

Bodvarsson, G.S., W. Boyle, R. Patterson, and D. Williams, 1999. Overview of scientific investigations at Yucca Mountain - the potential repository for high-level nuclear waste. Journal of Contaminant Hydrology 38:3-24.

Deutsch, C.V., and A.G. Journel, 1992. Gslib: Geostatistical software library and user's guide Oxford University Press, New York, New York.

Finsterle, S. 1999. Itough2 user's guide Report No. LBNL-40040. Lawrence Berkeley National Laboratory.

Finsterle, S., 2000. Using the continuum approach to model unsaturated flow in fractured rock. Water Resources Research 36:2055-2066.

Finsterle, S., and R.C. Trautz, 2001. Numerical modeling of seepage into underground openings. Mining Engineering 53:52-56.

Finsterle, S., C.F. Ahlers, R.C. Trautz, and P.J. Cook, 2003. Inverse and predictive modeling of seepage into underground openings. Journal of Contaminant Hydrology 62-63:89-109.

Fujimaki, H., and M. Inoue, 2003. A transient evaporation method for determining soil hydraulic properties at low pressure. Vadose Zone J 2:400-408.

Ho, C.K., 1997. Evaporation of pendant water droplets in fractures. Water Resources Research 33:2665-2671.

Knight, J.H., J.R. Philip, and R.T. Waechter, 1989. The seepage exclusion problem for spherical cavities. Water Resources Research 25:29-37.

505 LeCain, G.D. 1995. Pneumatic testing in 45-degree-inclined boreholes in ash-flow tuff near
506 superior, arizona Water-Resources Investigations Report 95-4073. U.S. Geological Survey,
507 Denver, Colorado.

508 Li, G.M., and C.-F. Tsang, 2003. Seepage into drifts with mechanical degradation. Journal of
509 Contaminant Hydrology 62:157-172.

510 Murray, F.W., 1966. On the computation of saturation vapor pressure. J. Appl. Meteor. 6:204.

511 Or, D., and T.A. Ghezzehei, 2000. Dripping into subterranean cavities from unsaturated fractures
512 under evaporative conditions. Water Resources Research 36:381-393.

513 Philip, J.R., 1989a. Asymptotic solutions of the seepage exclusion problem for elliptic-
514 cylindrical, spheroidal, and strip-shaped and disc- shaped cavities. Water Resources
515 Research 25:1531-1540.

516 Philip, J.R., 1989b. The seepage exclusion problem for sloping cylindrical cavities. Water
517 Resources Research 25:1447-1448.

518 Philip, J.R., J.H. Knight, and R.T. Waechter, 1989a. The seepage exclusion problem for
519 parabolic and paraboloidal cavities. Water Resources Research 25:605-618.

520 Philip, J.R., J.H. Knight, and R.T. Waechter, 1989b. Unsaturated seepage and subterranean holes
521 - conspectus, and exclusion problem for circular cylindrical cavities. Water Resources
522 Research 25:16-28.

523 Pruess, K., C. Oldenburg, and G. Moridis. 1999. Tough2 user's guide, version 2.0 LBNL-43134.
524 Lawrence Berkeley National Laboratory, Berkeley, Calif.

525 Rohsenow, W.M., and H. Choi, 1961. Heat, mass and momentum transfer Prentice-Hall Inc.,
526 Englewood Cliffs, New Jersey.

527 Trautz, R.C., and J.S.Y. Wang, 2001. Evaluation of seepage into an underground opening using
528 small- scale field experiments, yucca mountain, nevada. Mining Engineering 53:41-44.

529 Trautz, R.C., and J.S.Y. Wang, 2002. Seepage into an underground opening constructed in
530 unsaturated fractured rock under evaporative conditions. Water Resources Research
531 38:1188.

532 van Genuchten, M.T., 1980. A closed-form equation for predicting the hydraulic conductivity of
533 unsaturated soils. Soil Science Society of America Journal 44:892-898.

534 Wang, J.S.Y., R.C. Trautz, P.J. Cook, S. Finsterle, A.L. James, and J. Birkholzer, 1999. Field
535 tests and model analyses of seepage into drift. Journal of Contaminant Hydrology 38:323-
536 347.

537 Zhang, J.T., and B.X. Wang, 2002. Effect of capillarity at liquid-vapor interface on phase change
538 without surfactant. International Journal of Heat & Mass Transfer 45:2689-2694.

539 Zhang, J.T., B.X. Wang, and X.F. Peng, 2001. Thermodynamic aspect of the shift of concave
540 liquid-vapor interfacial phase equilibrium temperature and its effect on bubble formation.
541 International Journal of Heat and Mass Transfer 44:1681-1686.
542

Figures

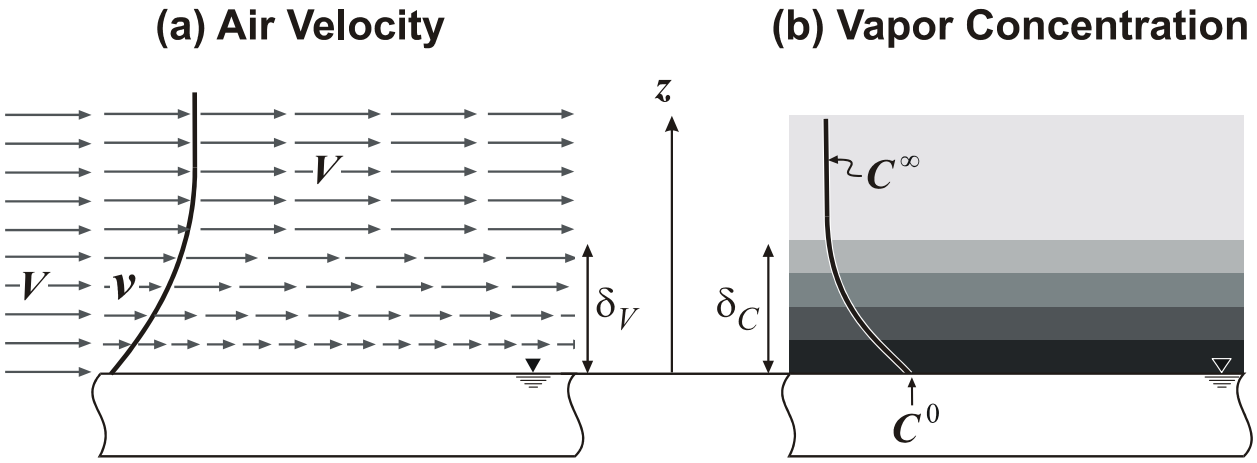

Fig. 1. Schematic description of (a) air velocity and (b) vapor concentration profiles above a free water surface

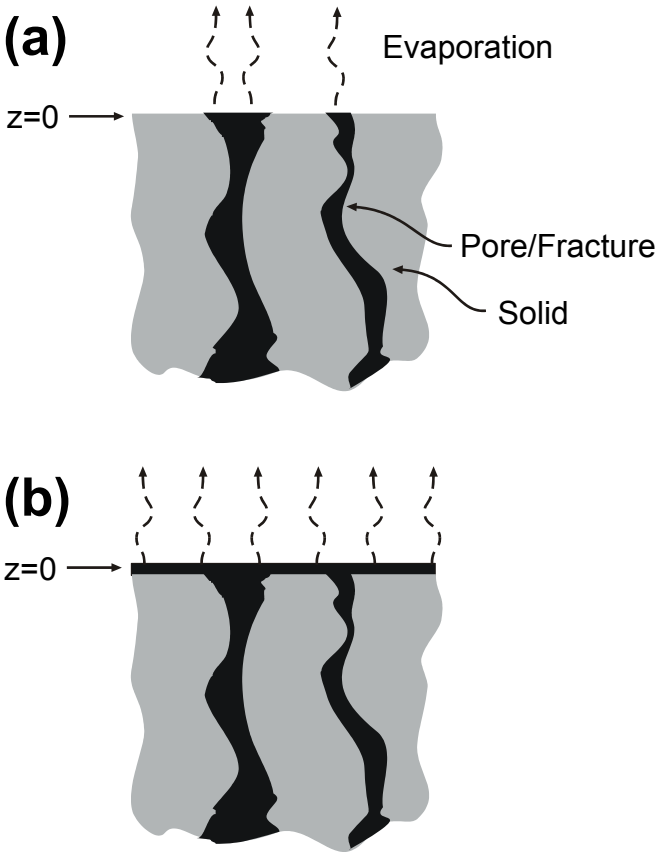

Fig. 2. Evaporating surface area of a porous medium: (a) partitioning of the surface into non-evaporating solid and evaporating pores; (b) proposed approach of uniform gas-phase surface.

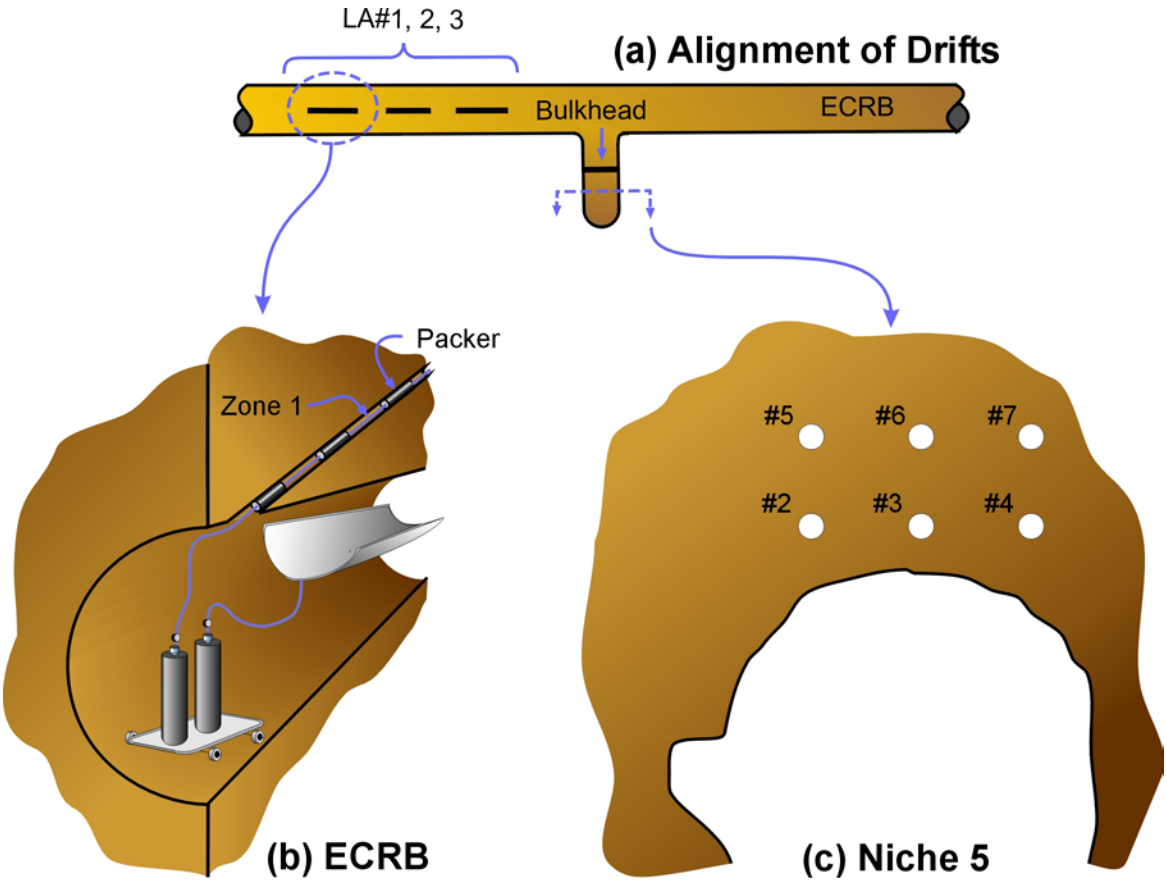

Fig. 3. Schematic alignment of tunnels and boreholes: (a) parts of the Exploratory Studies Facility (ESF) tunnel and Enhanced Characterization of the Repository Block (ECRB) cross-drift; (b) liquid release test setup in the Cross Drift, including liquid release intervals and liquid injection and seepage collection equipment; and (c) vertical section of Niche 5 along with location of all the test boreholes.

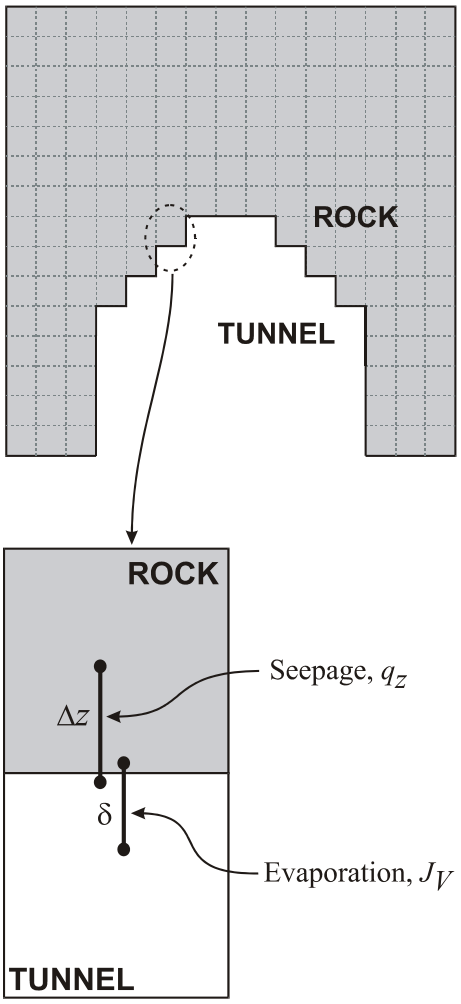

Fig. 4. Schematic description of the seepage and evaporation connections between nodes that represent the rock of the tunnel wall and the tunnel.

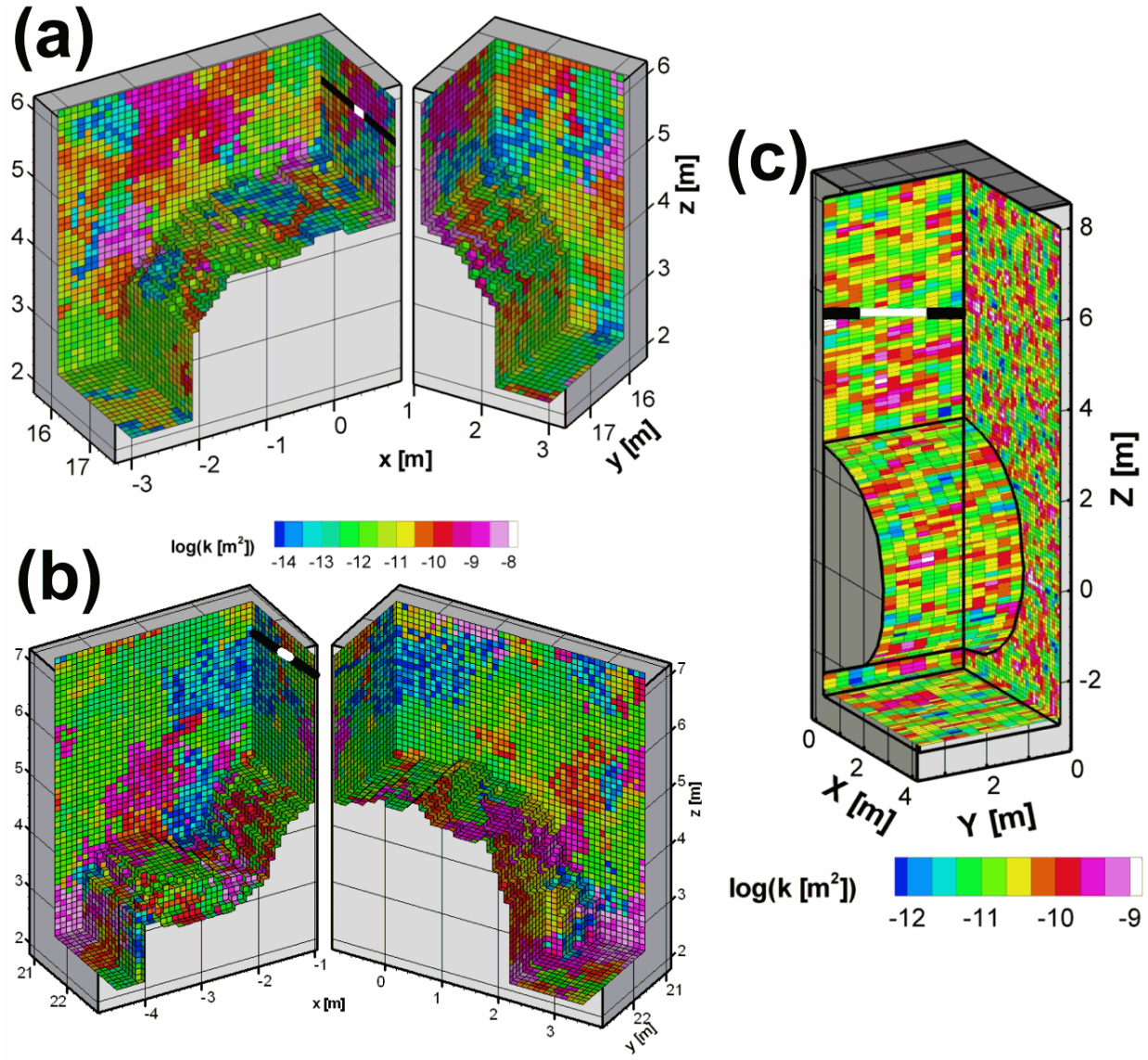

Fig. 5. Numerical meshes of (a) Niche 5 with borehole #4, (b) Niche 5 with borehole #5, and (c) the Cross Drift, along with a typical realization of the correlated stochastic permeability field. Bold black lines denote the liquid-release boreholes, and the white section in the middle of the boreholes is the injection interval.

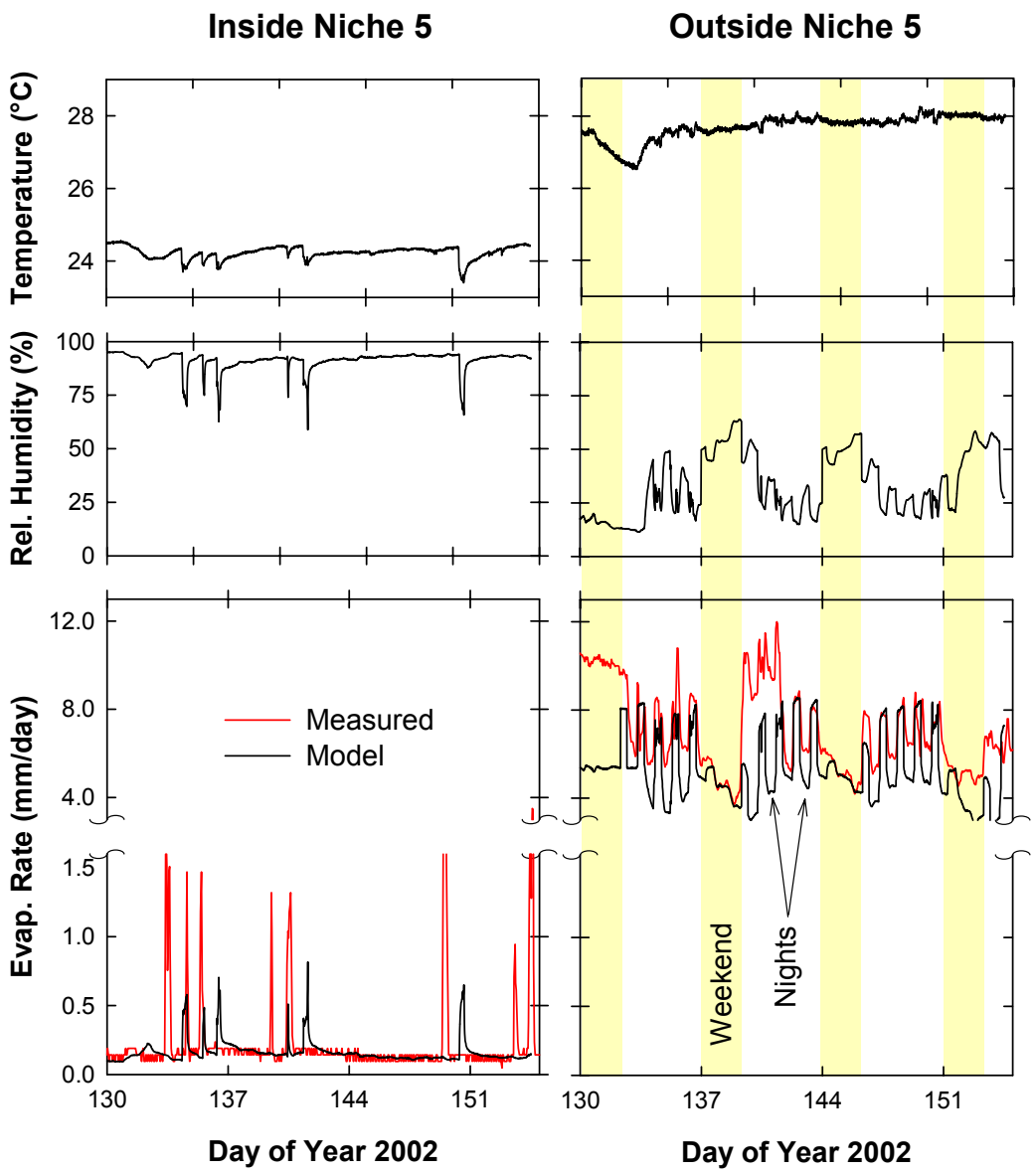

Fig. 6. Temperature, humidity, and evaporation rate data, along with model fit of the evaporation data

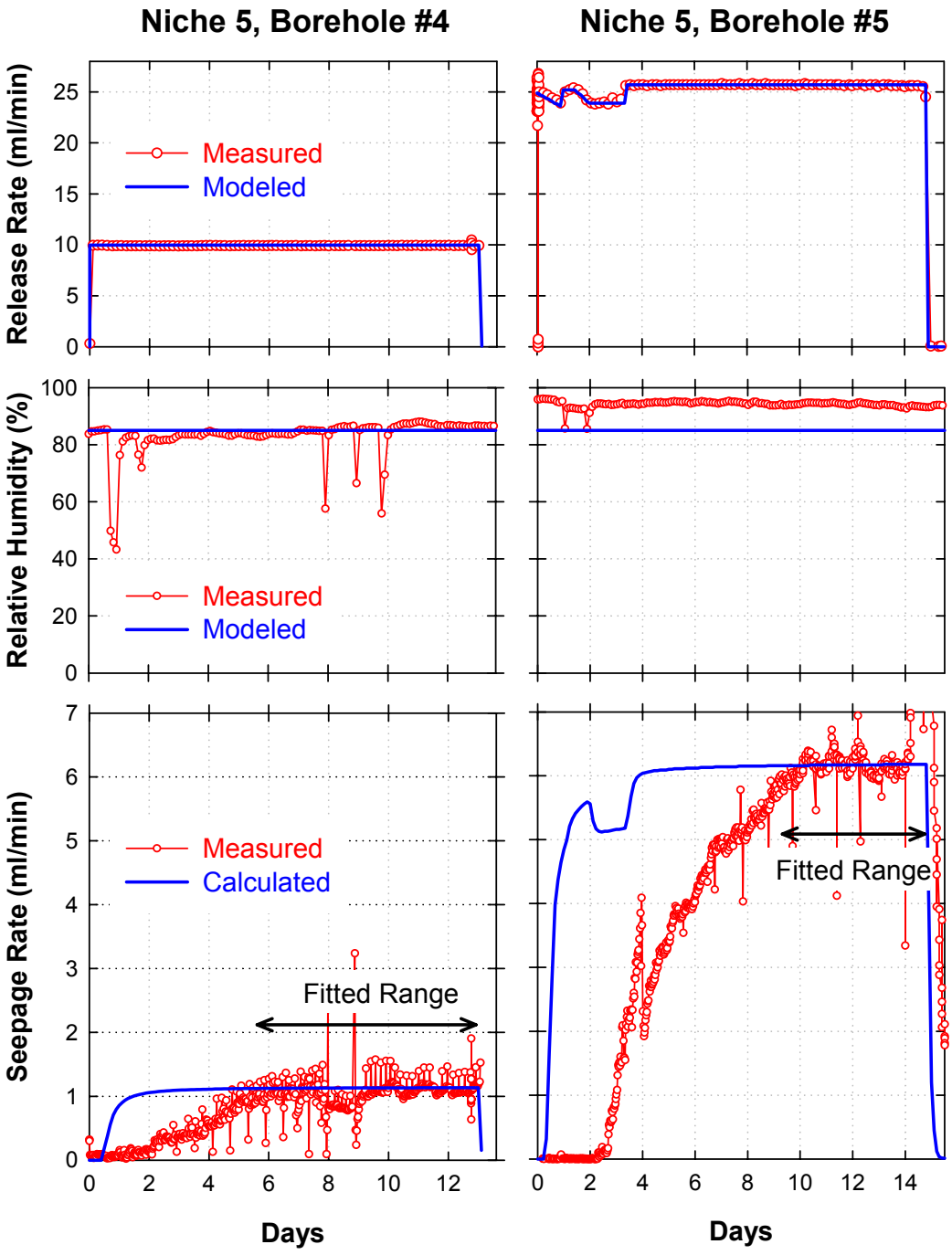

Fig. 7. Calibration of seepage-rate data from liquid-release tests conducted in Niche 5. Calculated seepage rate curves show only one of the multiple inversions.

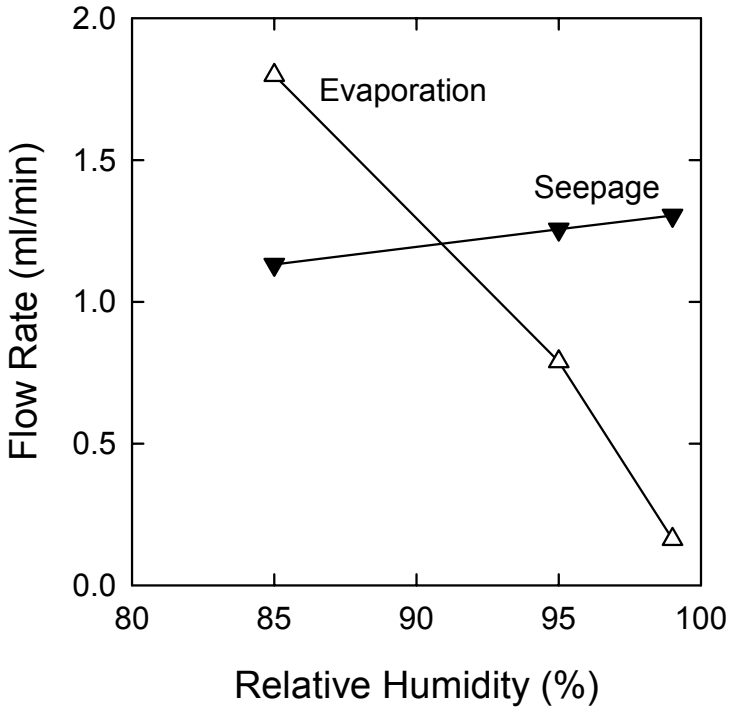

Fig. 8. Effect of high relative humidity on evaporation and seepage rates.

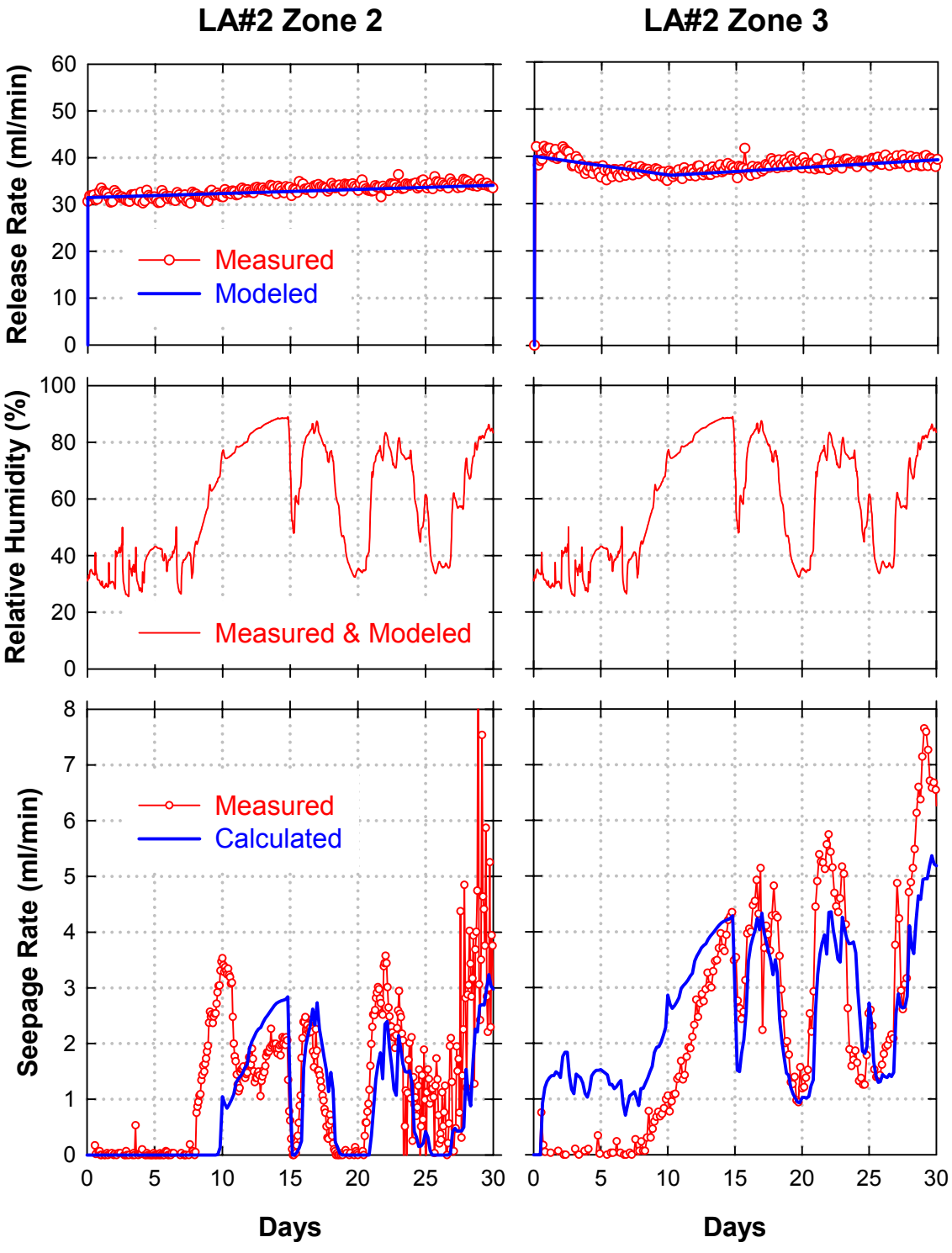

Fig. 9. Calibration of seepage-rate data from liquid-release tests conducted in the ECRB Cross Drift. Calculated seepage rate curves show only one of the multiple inversions.

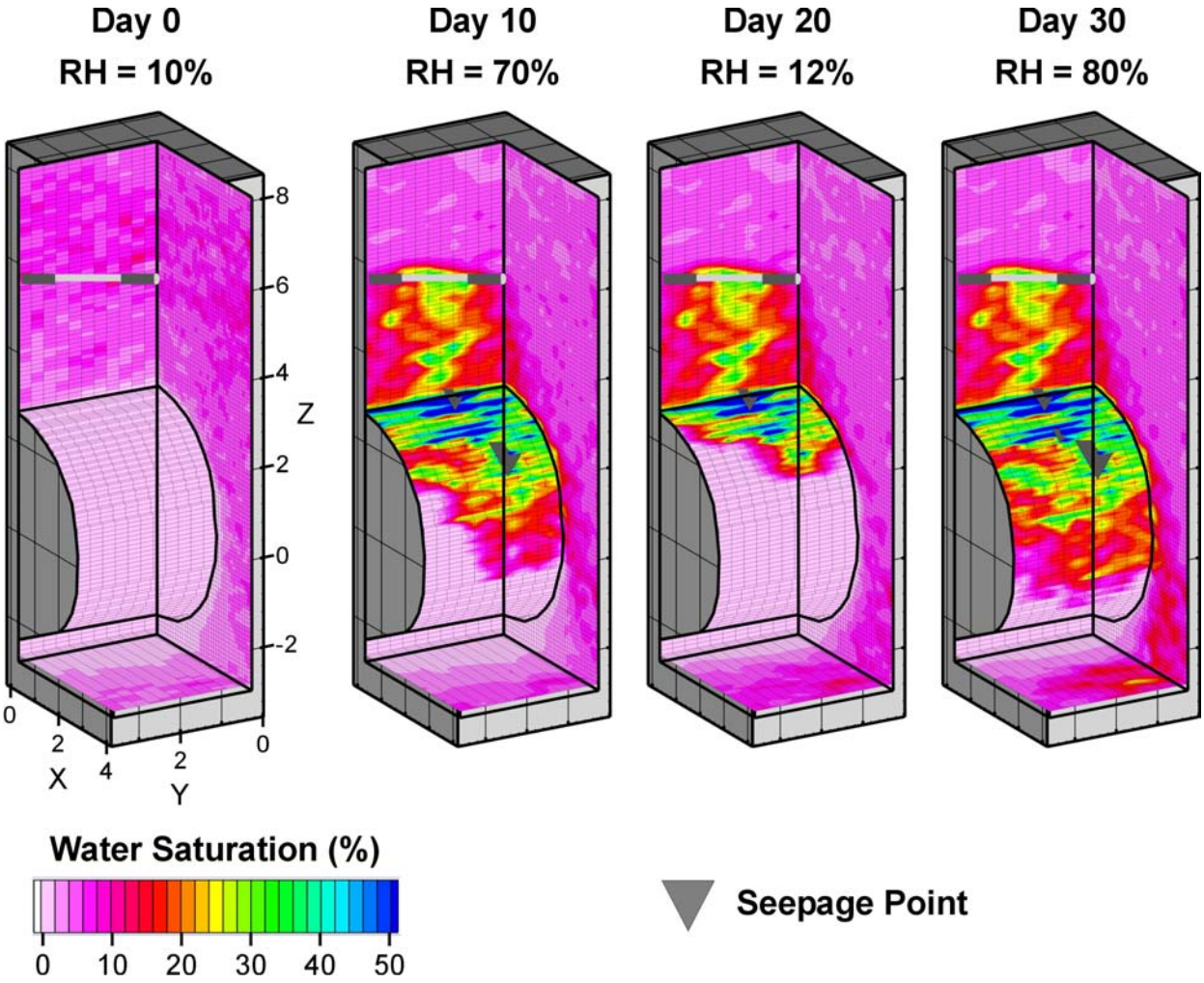

Fig. 10. Liquid saturation distribution simulated with model calibrated against seepage-rate data from liquid-release tests conducted in the Cross Drift borehole LA#2, Zone 2 at 0, 10, 20, and 30 days after the start of the liquid release tests. Note the correlation of tunnel wall wetness to tunnel relative humidity.